



Research
Wastewater Treatment—Article

Sustainable Generation of Sulfate Radicals and Decontamination of Micropollutants via Sequential Electrochemistry



Wentian Zheng^a, Shijie You^{b,*}, Yuan Yao^c, Nanqi Ren^b, Bin Ding^d, Fang Li^{a,e}, Yanbiao Liu^{a,e,*}

^aCollege of Environmental Science and Engineering, Donghua University, 2999 North Renmin Road, Shanghai 201620, China

^bState Key Laboratory of Urban Water Resource and Environment, School of Environment, Harbin Institute of Technology, Harbin 150090, China

^cMIT Key Laboratory of Critical Materials Technology for New Energy Conversion and Storage, School of Chemistry and Chemical Engineering, Harbin Institute of Technology, Harbin 150080, China

^dInnovation Center for Textile Science and Technology, College of Textiles, Donghua University, Shanghai 200051, China

^eShanghai Institute of Pollution Control and Ecological Security, Shanghai 200092, China

ARTICLE INFO

Article history:

Received 6 August 2022

Revised 22 October 2022

Accepted 5 December 2022

Available online 10 January 2023

Keywords:

Advanced oxidation

Chain reaction

Sulfate radical

Micropollutants

Sequential electrochemistry

ABSTRACT

The removal of emerging micropollutants in the aquatic environment remains a global challenge. Conventional routes are often chemically, energetically, and operationally intensive, which decreases their sustainability during applications. Herein, we develop an advanced chemical-free strategy for micropollutants decontamination that is solely based on sequential electrochemistry involving ubiquitous sulfate anions in natural and engineered waters. This can be achieved via a chain reaction initiated by electrocatalytic anodic sulfate (SO_4^{2-}) oxidation to produce persulfate ($\text{S}_2\text{O}_8^{2-}$) and followed by a cathodic persulfate reduction to produce sulfate radicals ($\text{SO}_4^{\cdot-}$). These $\text{SO}_4^{\cdot-}$ are powerful reactive species that enable the unselective degradation of micropollutants and yield SO_4^{2-} again in the treated water. The proposed flow-through electrochemical system achieves the efficient degradation (100%) and total organic carbon removal (65.0%) of aniline under optimized conditions with a single-pass mode. We also reveal the effectiveness of the proposed system for the degradation of a wide array of emerging micropollutants over a broad pH range and in complex matrices. This work provides the first proof-of-concept demonstration using ubiquitous sulfate for micropollutants decontamination, making water purification more sustainable and more economical.

© 2023 THE AUTHORS. Published by Elsevier LTD on behalf of Chinese Academy of Engineering and Higher Education Press Limited Company. This is an open access article under the CC BY-NC-ND license (<http://creativecommons.org/licenses/by-nc-nd/4.0/>).

1. Introduction

Recently, the widespread occurrence of organic micropollutants in aquatic environments has become a global environmental issue. Micropollutants—also known as emerging contaminants—comprise a broad category of natural and/or anthropogenic substances [1,2], including endocrine-disrupting chemicals, pharmaceutical and personal care products, and so forth. Micropollutants are usually present in water at trace concentrations ranging from nanograms to micrograms per liter ($\text{ng}\cdot\text{L}^{-1}$ to $\mu\text{g}\cdot\text{L}^{-1}$). Their limited concentration and vast diversity complicate the associated detection techniques and pose formidable challenges for wastewater treatment [3]. Existing wastewater treatment plants are not specifically designed to remove micropollutants. Hence, the

abovementioned micropollutants may re-enter aquatic environments due to their persistency, high toxicity, incomplete removal, or/and continuous introduction. Moreover, it should be noted that the concentration of micropollutants is generally several orders of magnitude lower than that of coexisting substances in natural and engineered water systems [4]. These coexisting substances may change the degradation pathways of target micropollutants, thereby affecting their transformation process and removal efficiency [5,6].

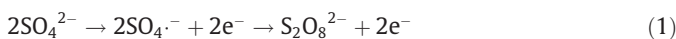
Among these coexisting substances, sulfates are the most common anions, with a typical concentration on the level of dozens to hundreds of milligrams per liter ($\text{mg}\cdot\text{L}^{-1}$) [7]. Unlike other anions, sulfate anions can be converted under certain conditions into highly reactive sulfate radicals ($\text{SO}_4^{\cdot-}$) [8], which can be employed to degrade various refractory organic contaminants in water [5,9,10]. Nonetheless, most reported pathways for $\text{SO}_4^{\cdot-}$ generation are associated with the activation of persulfate, and all of them

* Corresponding authors.

E-mail addresses: sjyou@hit.edu.cn (S. You), yanbiaoliu@dh.u.edu.cn (Y. Liu).

exhibit specific limitations [11–13]. Transition metal catalysts are the most widely used catalysts for persulfate activation due to their effectiveness [14]. However, this technique can produce secondary pollution by dissolving metal ions into the water [15,16], and it requires large amounts of chemicals for catalyst preparations. Ultraviolet light, heat, electricity, and ultrasound can also be used to activate persulfate [17,18], but these technologies are costly and energy-intensive, and are thus only suitable for small volumes of wastewater. Direct and sole utilization of the sulfate anions that are ubiquitous in water to produce $\text{SO}_4^{\cdot-}$ would undoubtedly provide a sustainable and revolutionary strategy for water purification.

In fact, sulfate anions can be oxidized to persulfates under an electric field (Eq. (1)) [19], and persulfates can be activated by electrocatalysis on an appropriate cathode to form sulfate radicals (Eq. (2)) [20]. Therefore, it is theoretically feasible to sequentially convert SO_4^{2-} to $\text{S}_2\text{O}_8^{2-}$ and then to $\text{SO}_4^{\cdot-}$ by rationally designing a sequential electrochemical system. Such an advanced wastewater treatment system is highly desirable, since it does not require the addition of chemicals, uses only electric energy, and yields sulfate anions again in the treated water. This concept of persulfate generation from sulfate oxidation has been demonstrated in a recent report using a boron-doped diamond (BDD) plate electrode [21]. However, this route may not be feasible for practical applications due to the costly BDD electrode and limited mass transport. Likewise, the oxidation of sulfate to persulfate has been achieved on specific crystal planes of metal oxides (e.g., TiO_2 , WO_3 , and BiVO_4) [22]. Again, the preparation of such catalysts involves complex synthetic methods, posing a barrier to the large-scale implementation of this approach.



Herein, we report and demonstrate a flow-through electrochemical system in which the generation of $\text{S}_2\text{O}_8^{2-}$ and its transformation to $\text{SO}_4^{\cdot-}$ can be achieved via sequential electrochemistry. This flow-through design can maximize the contact between the reactants and the active sites of the electrodes, thereby outperforming conventional batch reactors. The key to such a system is a free-standing and three-dimensional (3D) porous anode consisting of a carbon nanotube (CNT) filter functionalized with titanium suboxides (TiSO) and a perforated titanium (Ti) foil cathode. The CNT-based membrane electrode has the capability to couple the electrochemical reaction with filtration, which improves the reaction kinetics. More importantly, this process does not require additional chemical reagents and runs solely on the ubiquitous SO_4^{2-} and electricity; thus, it is a novel strategy for sustainable environmental remediation.

2. Materials and methods

2.1. Chemicals and materials

Multi-walled CNTs were obtained from TimesNano Co., Ltd. (China). The polytetrafluoroethylene (PTFE) support membrane ($D = 47$ mm) was supplied by Millipore (Omnipore, JMWP, USA). All solutions were prepared using ultra-pure water produced from a Milli-Q Direct 8 purification system (18.2 M Ω ·cm; Merck KGaA, Germany). Ethanol ($\text{C}_2\text{H}_5\text{OH}$; $\geq 96\%$), sodium sulfate (Na_2SO_4 ; $\geq 98\%$), sodium silicate (Na_2SiO_3 ; $\geq 98\%$), sodium chloride (NaCl; $\geq 98\%$), sodium perchlorate (NaClO_4 ; $\geq 98\%$), 5,5-dimethyl-1-pyrroline-n-oxide (DMPO, $\text{C}_6\text{H}_{11}\text{NO}$; $\geq 97\%$), tert-butyl alcohol (TBA, $\text{C}_4\text{H}_{10}\text{O}$; $\geq 98\%$), methanol (CH_3OH ; $\geq 98\%$), methylene blue ($\text{C}_{16}\text{H}_{18}\text{ClN}_3\text{S}$; molecular weight (MW) = 319.85 g·mol $^{-1}$) and methyl orange

($\text{C}_{14}\text{H}_{14}\text{N}_3\text{SO}_3\text{Na}$; MW = 327.33 g·mol $^{-1}$) were supplied by Sinopharm Chemical Reagent (China). Tetracycline ($\text{C}_{22}\text{H}_{24}\text{N}_2\text{O}_8$; $\geq 98\%$), sulfamethoxazole (SMX, $\text{CHN}_3\text{O}_3\text{S}$; $\geq 98\%$), and bisphenol A ($\text{C}_{15}\text{H}_{16}\text{O}_2$; $\geq 96\%$) were provided by Sigma-Aldrich (China).

2.2. Characterization

The crystal phase characteristics of the as-prepared samples were assessed by means of X-ray diffraction (XRD; D/max-2550VB+/PC, Rigaku Co., Ltd., Japan) with Cu K α radiation. The electrochemical properties of the CNT-TiSO nanohybrid filters were determined by means of linear sweep voltammetry (LSV), electrochemical impedance spectroscopy (EIS), and cyclic voltammetry (CV) techniques using a three-electrode system (i.e., a CNT-TiSO filter, whose preparation method is described in Appendix A Section S1, as a working electrode; a perforated titanium sheet as a counter electrode; and an Ag/AgCl reference electrode). EIS analysis was conducted at an amplitude of 5 mV over the frequency range of 0.1–100.0 kHz. LSV and CV were performed in 50 mmol·L $^{-1}$ Na_2SO_4 electrolyte at a scan rate of 10 mV·s $^{-1}$. The morphology of the as-prepared samples was characterized using a field-emission scanning electron microscope (FESEM; S-4800, Hitachi, Japan).

2.3. Experimental setup and operation

The electrochemical oxidation of organic pollutants was carried out using a Whatman polycarbonate filter case with electrochemical modifications (Fig. S1 in Appendix A). The difference between systems I and II is the sequence in which the solution flows through the cathode and anode, with different sequences resulting in different key active species. The schematic illustration of systems I and II is shown in Fig. S1. In system I, the water first flows through the Ti cathode and then through the CNT-TiSO anode. In system II, the water first flows through the CNT-TiSO anode, in which persulfate is generated, and then flows through the Ti cathode. To achieve filter adsorption saturation, 360 mL of aniline solution (0.1 mmol·L $^{-1}$) was allowed to flow through an Ismatec ISM833C peristaltic pump (Ismatec, Switzerland) for 4.5 h to explore the adsorption performance of CNT-TiSO for aniline (Fig. S2 in Appendix A). Subsequently, the aniline degradation experiments were carried out. Chronopotentiometric electrolysis was performed using a CHI660E electrochemical workstation (Shanghai Chenhua Technology, China) in the galvanostatic mode at a current density of 2.5 mA·cm $^{-2}$. The effects of the electrolyte, sulfate concentration, and flow rate on the aniline degradation kinetics were systematically evaluated. For the batch experiment, the CNT-TiSO filter anode, a Ti sheet cathode, and an Ag/AgCl reference electrode were transferred into a beaker containing 50 mL of aniline (0.1 mmol·L $^{-1}$) and Na_2SO_4 solution (50 mmol·L $^{-1}$) at 2.5 mA·cm $^{-2}$. For selected aniline degradation experiments, methanol was added to the Na_2SO_4 electrolyte to serve as a radical scavenger in order to terminate radical-induced reactions.

2.4. Analytical methods

The concentration of aniline and other refractory contaminants was detected using high-performance liquid chromatography (HPLC) with a poroshell 120 EC-C18 column (150 mm \times 4.6 mm, 3.5 μm , Waters XBridge, USA) and an ultraviolet-visible (UV-vis; Agilent, USA) detector. The as-generated radicals were trapped with DMPO and measured using a Bruker EMX nano Bench-Top electron paramagnetic resonance (EPR) spectrometer (Bruker, Germany). Persulfate concentration was determined using a potassium iodide (KI) method, in which the KI reacts with hydrogen peroxide (H_2O_2) and persulfate. To further differentiate the H_2O_2 and persulfate, the concentration of H_2O_2 was measured using

potassium titanium oxalate, which does not react with persulfate (Section S2 in Appendix A). The aniline degradation intermediates were determined by means of liquid chromatography–tandem mass spectrometry (LC–MS; PR-LCMS-2020, Shimadzu, Japan). The total organic carbon (TOC) was determined using a Multi N/C3 100 TOC/TN analyzer (Analytik Jena, Germany).

2.5. Density functional theory computation

Density functional theory (DFT) calculations were conducted with Gaussian 09 software based on the gradient-corrected Becke three-parameter Lee–Yang–Parr (B3LYP) functional. For geometry optimization and frequency calculations, the 6–31+G(d) basis set was selected for all elements. To obtain more accurate energies, single energy calculations were subsequently conducted with the 6–311+G(3df, 2p) basis set according to the optimized geometries. The solvation effect was considered with implicit water solvation using the solvation model based on density (SMD), a continuum solvation model based on the quantum mechanical charge density of a solute molecule interacting with a continuum description of the solvent [23]. The profiles of the Gibbs free energy of activation versus the electrode potential for direct electron transfer reactions were determined using the Marcus theory.

3. Results and discussion

3.1. Anodic persulfate production

We first employed the XRD technique to investigate the crystal structure of the anode, which was a CNT–TiSO nanohybrid filter. Since the intensity of the carbon reflections was too strong and covered other characteristic XRD peaks (Fig. S3 (a) in Appendix A), the XRD pattern of the CNT–TiSO was enlarged. Fig. S3(b) in Appendix A shows the dominant peaks of Ti_4O_7 and minor peaks originating from the Ti_5O_9 crystal (PDF#50–0787), possibly due to their similar formation temperatures. Both Ti_4O_7 and Ti_5O_9 are the most conductive titanium oxides and thus have excellent physiochemical attributes for electrooxidation applications [24].

To better understand the chemical composition of the filter surface, high-resolution X-ray photoelectron spectroscopy were obtained (Fig. S4 in Appendix A). The binding energies of 464.3, 463.6, 458.6, and 458.2 eV ($1 \text{ eV} = 1.602176 \times 10^{-19} \text{ J}$) correspond to the characteristic peaks of Ti^{4+} ($2p_{1/2}$), Ti^{3+} ($2p_{1/2}$), Ti^{4+} ($2p_{3/2}$), and Ti^{3+} ($2p_{3/2}$), respectively [25]. In addition, a thorough characterization was conducted to investigate the electrochemical behavior of the CNT–TiSO nanohybrid filter. Fig. 1 showed the electrochemical characterization of CNT–TiSO and persulfate concentrations at different times, electrolytes, and current densities. The charge transfer resistance of the CNT–TiSO filter electrode was first characterized by means of EIS. As shown in Fig. 1(a), the circular arc related to the CNT–TiSO filter electrode exhibits a lower radius than that of the pristine CNT filter, implying that the addition of TiSO remarkably decreases the interfacial resistance (58 vs 47 Ω) and accelerates the electron transfer process. Some anode materials may be problematic for scale-up application due to their low oxygen evolution potential (OEP; the minimal potential for an oxygen evolution reaction) during an electrochemical oxidation process [26]. For example, aromatic hydrocarbons typically have a high OEP (e.g., 2.8 V vs saturated calomel electrode (SCE) for benzene), making it difficult for them to be electrochemically oxidized by commercial electrodes with a lower OEP (< 2.8 V vs SCE). A high OEP can attenuate the side reactions of oxygen evolution, thereby improving the oxidation efficiency of contaminants and reducing energy consumption [27]. Thus, the electrochemical behavior of the as-synthesized filter was examined via LSV. As shown in Fig. 1(b), the addition of TiSO increased the OEP from 1.7 to 2.1 V vs Ag/AgCl, which exceeded the potential of the anodic reactions (2.0 V vs Ag/AgCl).

Tafel plots can be deemed a significant kinetic parameter to describe the underlying mechanism in detail. According to Section S3 and Fig. S5 in Appendix A, the CNT–TiSO filter showed a Tafel slope of $2.7 \text{ mV}\cdot\text{dec}^{-1}$, which was again lower than that of the sole CNT counterpart, suggesting that CNT–TiSO exhibits faster kinetics in electrochemical reactions. The lower Tafel slope may be associated with the rapid electrochemical interactions between CNT and TiSO and the excellent electric conductivity of TiSO [28].

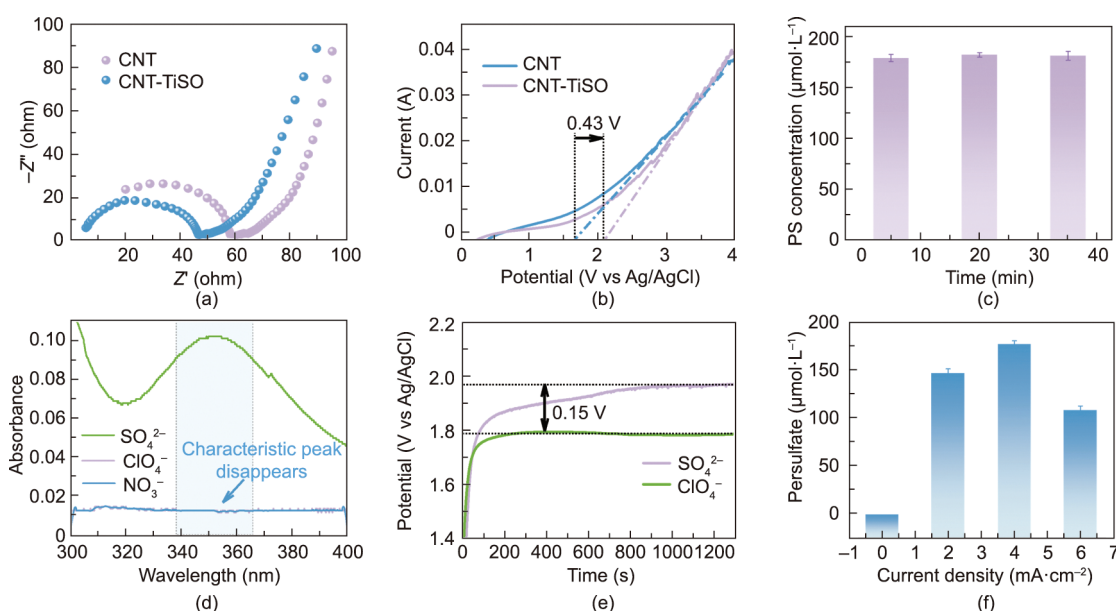


Fig. 1. (a) Nyquist diagrams and (b) LSV curves of CNT and CNT–TiSO. (c) Concentrations of persulfate anions formed at different times and (d) absorption spectra of triiodide ions formed by a persulfate–iodide reaction in different electrolytes (the blue shadow part indicates the characteristic peak). (e) Potentials during electrolysis in Na_2SO_4 and NaClO_4 electrolytes at a current density of $2.5 \text{ mA}\cdot\text{cm}^{-2}$. (f) Concentrations of persulfate formed at different current densities (the error bar represents one standard error of the mean of uncertainty in the synthetic data from triplicate experiments).

Subsequently, the efficacy of producing persulfate anions on the CNT-TiSO filter anode was evaluated. In the proposed electrochemical system, the sequence of water flow through different electrodes must be considered. Research has shown that sulfate anions can be transformed into persulfate ($S_2O_8^{2-}$) species at the anode under an appropriate electric field [19] and are then decomposed into sulfate radicals ($SO_4^{\cdot-}$) at the cathode [29]. We thus examined whether persulfate anions could be generated in a cathode-to-anode sequence (system I). As depicted in Fig. 1(c), a persulfate concentration of $180 \mu\text{mol}\cdot\text{L}^{-1}$ was obtained from the electrooxidation of the Na_2SO_4 electrolyte ($50 \text{ mmol}\cdot\text{L}^{-1}$) on the CNT-TiSO anode at a current density of $2.5 \text{ mA}\cdot\text{cm}^{-2}$, and the effluent persulfate yield remained constant throughout the reaction. However, no detectable persulfate was obtained using a pristine CNT anode, due to the relatively low OEP (Fig. S6 in Appendix A). Notably, the hydraulic residence time within the filter was $< 2 \text{ s}$ at a flow rate of $2.0 \text{ mL}\cdot\text{min}^{-1}$ (Section S4 in Appendix A), which is shorter than several state-of-the-art reports on aniline degradation (Table S1 in Appendix A). Since sulfate is the only sulfur-containing species in this system, it is reasonable to assume that SO_4^{2-} could be the precursor for $S_2O_8^{2-}$. As predicted, no peak signal associated with persulfate appeared when other sulfate-free electrolytes (e.g., NaNO_3 and NaClO_4) were used at a similar conductivity ($\sigma = 7240 \pm 100 \mu\text{S}\cdot\text{cm}^{-1}$) (Fig. 1(d)), highlighting the essential role of sulfate in persulfate generation. Besides, compared with the NaClO_4 electrolyte, the higher potential observed for the Na_2SO_4 electrolyte may originate from the increased electron flow during the electrochemical oxidation of sulfate (Fig. 1(e)) [30].

Since the electrolysis was carried out in the chronopotentiometry mode, a higher potential was needed to compensate for the charge consumption, so as to maintain a constant current density. Therefore, we considered two possible pathways for the electro-generation of persulfate from sulfate based on DFT calculation (Fig. 2(a)): ① SO_4^{2-} loses electrons to form $\text{SO}_4^{\cdot-}$, and then two $\text{SO}_4^{\cdot-}$ species couple to produce $S_2O_8^{2-}$ (Eqs. (3) and (4)) [8]; and/or ② SO_4^{2-} generates $S_2O_8^{4-}$, and then loses two electrons to produce $S_2O_8^{2-}$. The DFT results indicated that the structure of $S_2O_8^{4-}$ cannot be determined using geometry optimizations, suggesting that such a route can be excluded in the proposed electrochemical filtration system. The persulfate yield was highly correlated to the applied current density [31]. We further optimized the current density to maximize the persulfate yield. As shown in Fig. 1(f), the persulfate concentration increases gradually as the current density increases from 0 to $2.5 \text{ mA}\cdot\text{cm}^{-2}$ and decreases when the current density further increases to $3.0 \text{ mA}\cdot\text{cm}^{-2}$. This is related to the Gibbs free energy of the sulfate oxidation reaction at the anode potentials corresponding to the employed current densities.



Therefore, DFT calculations were used to calculate the activation energy (E_a ; $\text{kJ}\cdot\text{mol}^{-1}$) for the direct electron transfer (DET) reaction of sulfate oxidation. As indicated in Fig. 2(b), the E_a value

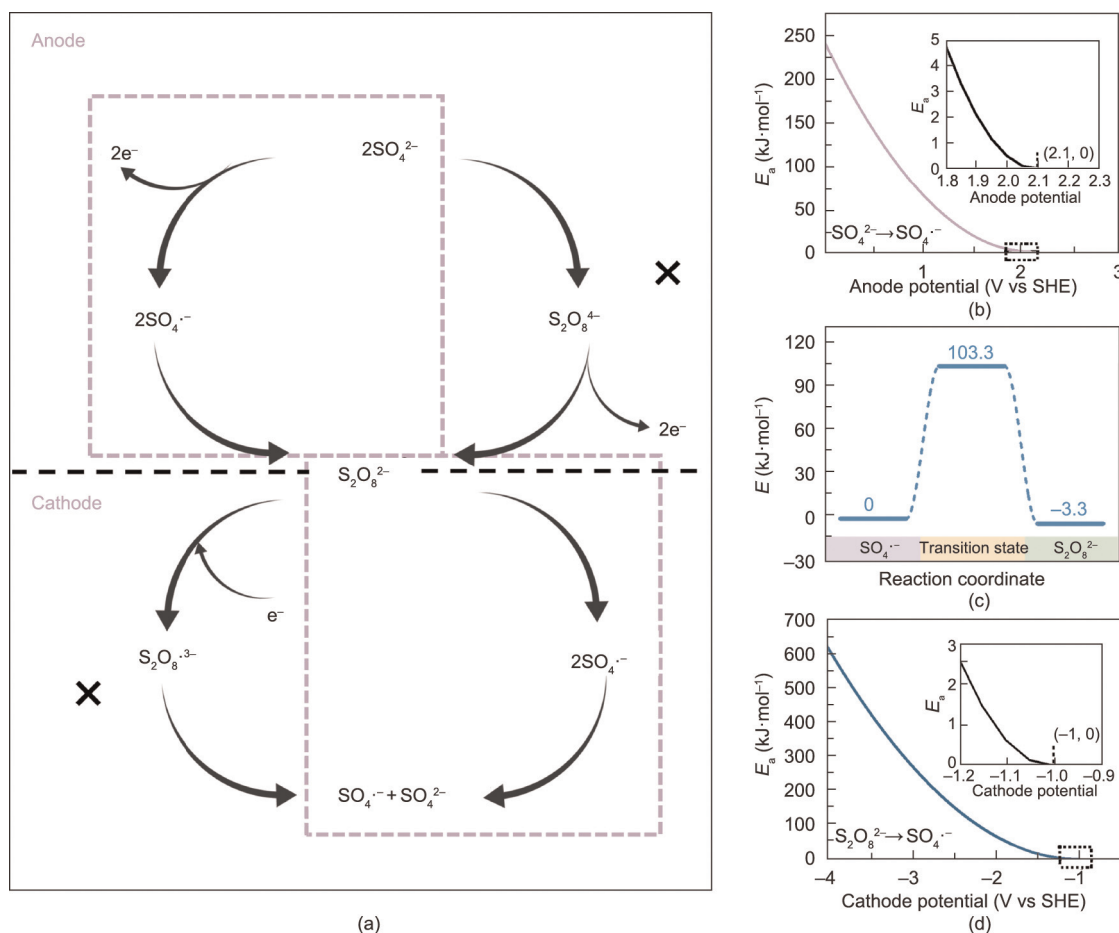


Fig. 2. (a) Possible reaction mechanism. (b) DFT-determined activation energy E_a vs the anode potential profile. (c) Free energy diagram for the reaction converting $\text{SO}_4^{\cdot-}$ into the $\text{S}_2\text{O}_8^{2-}$ anion. (d) DFT-determined E_a vs the cathode potential profile at room temperature.

gradually decreases with the anode potential (0–2.1 V vs standard hydrogen electrode (SHE)). The E_a value for sulfate oxidation to generate $\text{SO}_4^{\cdot-}$ (Eq. (3)) almost approaches $0 \text{ kJ}\cdot\text{mol}^{-1}$ at 2.1 V vs SHE (equivalent to 1.7 V vs Ag/AgCl), which is very close to the corresponding anode potential of 2.0 V vs Ag/AgCl at $2.5 \text{ mA}\cdot\text{cm}^{-2}$. This finding suggests that the DET reaction could easily occur, in line with the experimental results mentioned above. Thus, considering the persulfate yield and system efficiency, a current density of $2.5 \text{ mA}\cdot\text{cm}^{-2}$ was considered to be optimal for the proposed system. In addition, the transition state from $\text{SO}_4^{\cdot-}$ to $\text{S}_2\text{O}_8^{2-}$ anion (Eq. (4)) was determined. As shown in Fig. 2(c), the transition state is positioned $103.3 \text{ kJ}\cdot\text{mol}^{-1}$ higher than the $\text{SO}_4^{\cdot-}$ in terms of energy. This energy barrier is slightly high, but the reaction can still occur at ambient temperature according to the calculation results, indicating that this reaction is still dynamically favorable. Moreover, the convection-enhanced mass transport accelerates the reaction kinetics. Furthermore, $\text{SO}_4^{\cdot-}$ has similar energy to $\text{S}_2\text{O}_8^{2-}$, which implies that this reaction has a reversible nature.

3.2. Cathodic radical formation

To verify the transformation of persulfate anions to sulfate radicals, we let the water flow first through the CNT-TiSO anode and then flow through the Ti cathode (system II). The porous Ti sheet at the cathode ensures the plug-flow operation and enables the cleavage of the O–O bond of persulfate anions through electron transfer to induce the formation of sulfate radicals [20]. First, we analyzed the feasibility of this reduction reaction using DFT calculations. The Gibbs free energy of the persulfate activation profile as a function of the cathode potential is displayed in Fig. 2(d). It can be seen that the Gibbs free energy of activation for the DET reaction approaches 0 when the cathode potential is -1.0 V vs SHE (-1.4 V vs Ag/AgCl). The actual cathode potential at $2.5 \text{ mA}\cdot\text{cm}^{-2}$ is -1.0 V vs Ag/AgCl, indicating that this reaction is favorable. Second, the decomposition of persulfate was detected, and the formation pathway of the radicals was further explored. Fig. 3 showed the persulfate concentrations formed in different systems and identification of active species. As presented in Fig. 3(a), the persulfate concentration in the effluent of system II decreases significantly compared with that in the effluent of system I, which fully indicates that the decomposition of persulfate and the generation of sulfate radicals occur in system II. This claim is vividly supported by the characteristic signals of the DMPO– $\text{SO}_4^{\cdot-}$ adduct ($\alpha_{\text{H}} = 0.78 \text{ G}$, $\alpha_{\text{H}} = 1.48 \text{ G}$, $\alpha_{\text{H}} = 9.6 \text{ G}$, and $\alpha_{\text{N}} = 13.2 \text{ G}$), as determined by the EPR technique (Fig. 3(b)). Two plausible reaction pathways for $\text{SO}_4^{\cdot-}$ generation are further proposed: ① $\text{S}_2\text{O}_8^{2-}$ receives an electron to produce $\text{S}_2\text{O}_8^{3\cdot-}$ and then transforms into SO_4^{2-} and $\text{SO}_4^{\cdot-}$; and/or ② $\text{S}_2\text{O}_8^{2-}$ directly decomposes into two $\text{SO}_4^{\cdot-}$ (Eq. (2)), and

then the $\text{SO}_4^{\cdot-}$ is converted into SO_4^{2-} again (Eq. (5)). Pathway I can be excluded, because the structure of the $\text{S}_2\text{O}_8^{3\cdot-}$ species cannot be determined using geometry optimizations according to the DFT results.



Notably, a typical EPR spectrum of the DMPO–HO· adduct ($\alpha_{\text{N}} = \alpha_{\text{H}} = 14.9 \text{ G}$, $g = 2.0055$) with an intensity of 1:2:2:1 also emerges. We inferred three routes for the HO· formation: ① $\text{SO}_4^{\cdot-}$ reacts with water at all pH values to form HO· (Eq. (5)) [32]; ② HO· can be directly produced at the anode through the water oxidation reaction (Eq. (6)) [10]; and/or ③ hydrogen peroxide is electrochemically produced (Eq. (7)) [33] and can be further decomposed to HO· at the cathode (Eq. (8)) [34]. The first route was verified by adding TBA (a quencher of HO·, rate constant $k = 3.8 \times 10^8 \text{ L}\cdot(\text{mol}\cdot\text{s})^{-1}$ [35]) and *p*-hydroxybenzoic acid (a quencher of $\text{SO}_4^{\cdot-}$, $k = 2.5 \times 10^9 \text{ L}\cdot(\text{mol}\cdot\text{s})^{-1}$ [36,37]) to determine the concentrations of HO· and $\text{SO}_4^{\cdot-}$. The results indicated that the concentrations of HO· were relatively similar (2.5 vs $3.3 \mu\text{mol}\cdot\text{L}^{-1}$) and those of $\text{SO}_4^{\cdot-}$ were 40.1 and $1.2 \mu\text{mol}\cdot\text{L}^{-1}$, respectively. These observations suggest that $\text{SO}_4^{\cdot-}$ is the critical intermediate for the HO· production. The contribution of the second pathway is less, because only weak characteristic peaks are detected in system I (Fig. S7 in Appendix A). H_2O_2 is also detected on the anode, although its concentration is rather limited. This illustrates that the CNT-TiSO nanohybrid filter has the potential to be used in a two-electron water oxidation reaction. The reaction may inhibit the persulfate production reaction because of the competitive adsorption between water molecules and the SO_4^{2-} species. In the proposed electrochemical filtration system, the adsorption free energy of O^* (an intermediate state during water oxidation) may be lower than the persulfate generation energy, making persulfate formation more likely than H_2O_2 formation, according to the reported DFT calculation results [22]. A plausible underlying working mechanism for system II is proposed in Fig. 4.



3.3. System performance evaluation

Aniline—an important precursor for several commercial products and a common degradation intermediate during water treatment [38]—was selected as a model recalcitrant aqueous micropollutant to evaluate the system efficacy for organic degrada-

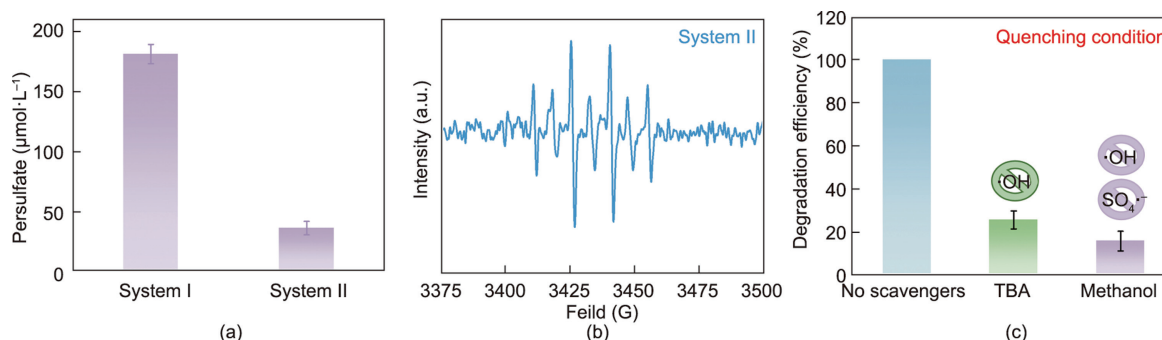


Fig. 3. (a) Concentrations of persulfate formed in systems I and II, (b) EPR spectra of CNT-TiSO in system II, and (c) degradation efficiency of aniline before and after adding TBA or methanol. Experimental conditions: $J = 2 \text{ mL}\cdot\text{min}^{-1}$, $[\text{aniline}]_0 = 0.1 \text{ mmol}\cdot\text{L}^{-1}$, $\text{pH} = 6.0$, $[\text{Na}_2\text{SO}_4]_0 = 50 \text{ mmol}\cdot\text{L}^{-1}$, current density = $2.5 \text{ mA}\cdot\text{cm}^{-2}$, $[\text{TBA}]_0 = [\text{methanol}]_0 = 100 \text{ mmol}\cdot\text{L}^{-1}$. The error bar represents one standard error of the mean of uncertainty in the synthetic data from triplicate experiments.

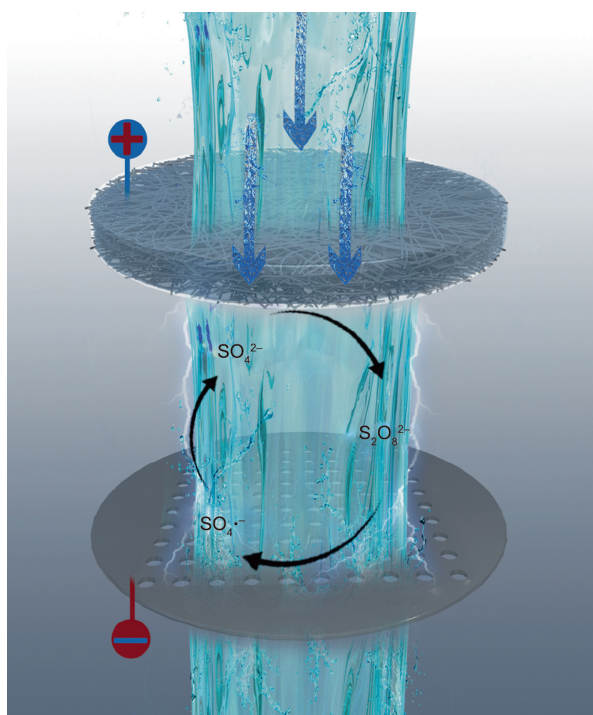


Fig. 4. Illustration of the working mechanism for system II.

tion. As shown in Fig. 5(a), only 33.5% aniline degradation is observed in the single-pass mode in system I, which may be attributed to the limited oxidative capability of persulfate generated *in situ*. Nevertheless, by spiking a similar persulfate concentration via system I (without exerting an electric field), only 23.7% aniline removal is achieved. This result suggests that *in situ*-generated persulfate possesses an enhanced oxidation ability, possibly because the active species produced at the anode, such as $\text{SO}_4^{\cdot-}$ and $\text{HO}\cdot$, can contribute to the electrochemical oxidation of aniline [8]. In stark contrast, system II demonstrates evidently increased aniline degradation kinetics, with complete aniline removal in a single pass, because the change of electrode sequence alters the active species acting on the aniline degradation from

persulfate in system I to radicals in system II. In addition, the removal efficiency of system II by the external spiking of a similar concentration of persulfate was slightly lower than that of the persulfate generated *in situ* (92.5% vs 100%), which further confirmed the outstanding performance of the proposed technology. The change in TOC of aniline was compared between systems I and II (Fig. 5(b)), and the results suggest enhanced TOC removal in system II (63.2%–65.0%) compared with system I (25.0%–25.6%).

The aniline degradation mechanism was further analyzed. To investigate whether the aniline oxidation reaction proceeds via the DET pathway, we recorded a CV scan (Fig. S8 in Appendix A). The obtained results exhibited no obvious oxidation current compared with that attained in an aniline-free solution with *ex situ* spiked aniline, suggesting the electrochemical inactivity of aniline within this potential range. Alternatively, it is most likely that aniline is oxidized indirectly by reactive species. To identify these reactive species, we performed chemical quenching experiments by spiking with different radical scavengers (i.e., TBA and methanol). The addition of 100 $\text{mmol}\cdot\text{L}^{-1}$ TBA or methanol suppresses the aniline degradation efficiency from 100% to 25.5% or 15.6%, respectively (Fig. 3(c)), suggesting that both $\text{SO}_4^{\cdot-}$ and $\text{HO}\cdot$ contribute to the aniline degradation. The corresponding concentrations of $\text{HO}\cdot$ and $\text{SO}_4^{\cdot-}$ and their contributions to aniline degradation were 20.5 $\mu\text{mol}\cdot\text{L}^{-1}$ (29.5%) and 48.9 $\mu\text{mol}\cdot\text{L}^{-1}$ (70.5%). To further verify whether the dominant product of the anodic reaction is persulfate, the concentrations of $\text{HO}\cdot$ and $\text{SO}_4^{\cdot-}$ in system I were determined to be 8.4 and 10.9 $\mu\text{mol}\cdot\text{L}^{-1}$, respectively. It is well-known that these radicals ($\text{SO}_4^{\cdot-}$, redox potential $E^0 = 2.6\text{--}3.1$ V vs SHE; $\text{HO}\cdot$, $E^0 = 1.9\text{--}2.7$ V vs SHE) possess much higher oxidation capacity than persulfate ($E^0 = 2.01$ V vs SHE) [39,40]. These results further verify the decomposition of persulfate at the cathode to induce the formation of more reactive radicals. In addition, it has been reported that certain redox-active polymeric intermediates, such as benzoquinone, may form during the electrochemical oxidation of aniline. These intermediates may undergo nucleophilic addition with persulfate to initiate the production of reactive oxygen species, which in turn improves the degradation efficiency of aniline [41]. However, the formation of benzoquinone cannot be traced by determining the intermediates in both systems because of the improper electrochemical environment for benzoquinone generation or extremely low yield, which lower than detection limit (Fig. S9 in Appendix A). Therefore, this pathway can be excluded as well.

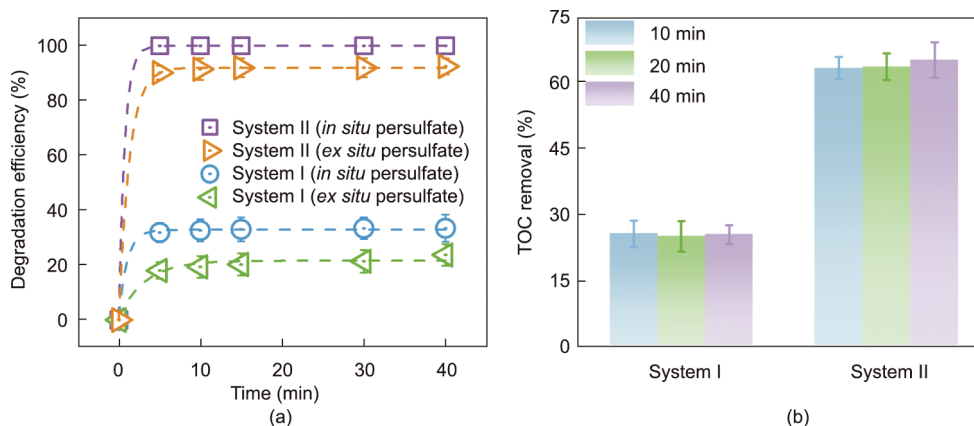


Fig. 5. (a) Degradation efficiency of aniline and (b) TOC removal in different systems. Experimental conditions: $J = 2$ $\text{mL}\cdot\text{min}^{-1}$, $[\text{aniline}]_0 = 0.1$ $\text{mmol}\cdot\text{L}^{-1}$, $\text{pH} = 6.0$, $[\text{Na}_2\text{SO}_4]_0 = 50$ $\text{mmol}\cdot\text{L}^{-1}$, current density = 2.5 $\text{mA}\cdot\text{cm}^{-2}$, $[\text{persulfate}]_0 = 180$ $\mu\text{mol}\cdot\text{L}^{-1}$. The error bar represents one standard error of the mean of uncertainty in the synthetic data from triplicate experiments.

3.4. Role of TiSO in sulfate oxidation

Previous studies suggest that sulfate can be converted into $\text{SO}_4^{\cdot-}$ within a narrow pH range [22]. Direct electron transfer from SO_4^{2-} to the anode (Faradaic process) and indirect oxidation of SO_4^{2-} by physisorbed $\text{HO}\cdot$ (non-Faradaic process) are responsible for this SO_4^{2-} oxidation [30]. Sulfate ions can be electrochemically activated via the direct and/or indirect discharge of SO_4^{2-} and/or HSO_4^- at the anode. Sulfate also exists in the form of HSO_4^- , which provides an additional channel for $\text{SO}_4^{\cdot-}$ generation (non-Faradaic process) under acidic pH conditions (Eqs. (9) and (10)) [30]. However, it has been reported that this route is also accessible in pH-neutral solutions due to the porous structure of TiSO, in which a low pH environment can be created in the local zones of solid/liquid interfaces [30]. This environment is favorable for sulfate activation to produce $\text{SO}_4^{\cdot-}$ even when the bulk solution has a neutral pH. Thus, we measured the local pH of TiSO. The pH value declines dramatically to 2.5 when the electrolysis ends up in 40 min. According to a previous report, the sodium sulfate solution at pH 2.5 contains approximately 20% HSO_4^- [30]. In addition to measuring the local pH directly, an attempt was made to theoretically calculate the local pH during electrolysis (Fig. S10 and Section S5 in Appendix A). According to the results of the calculations, it can be inferred that the local pH within the pores of TiSO can be kept acidic during the electrolysis process.



The electric double-layer structure may contribute to the adsorption of positively charged protons in the apertures, since TiSO exhibits capacitive characteristics originating from its developed porous structure and high surface area [24]. Moreover, the H^+ diffusion coefficient in a porous medium would be significantly decreased compared with that in the bulk solution, according to the calculation results given in Section S5. Hence, the accumulated H^+ ions within the pores of TiSO promote the combination of H^+ and SO_4^{2-} to produce HSO_4^- , providing another pathway to form $\text{SO}_4^{\cdot-}$ [30].

3.5. Importance of a sulfate electrolyte

To highlight the essential role played by the Na_2SO_4 electrolyte, we also explored the use of other common electrolytes (e.g., nitrate, chloride, and silicate) with the same conductivity ($\sigma = 7240 \pm 100 \mu\text{S}\cdot\text{cm}^{-1}$). As shown in Appendix A Fig. S11(a), sodium nitrate and sodium silicate electrolytes significantly reduce the aniline degradation kinetics. Since these inert electrolytes fail to generate reactive species in the electrooxidation reaction, only about 10% aniline degradation is achieved. The chloride electrolyte demonstrates moderate reduction of the aniline degradation (53.8%). Chloride oxidation at the anode surface generates chloride radicals, which collectively contribute to the aniline degradation. The addition of TBA (a quencher of chloride radicals; $k = 1.9 \times 10^9 \text{ L}\cdot(\text{mol}\cdot\text{s})^{-1}$) inhibits the degradation of aniline from 53.8% to 6.6%, further confirming the existence of chloride radicals. Unfortunately, compared with $\text{HO}\cdot$ and $\text{SO}_4^{\cdot-}$, the chloride radicals possess much weaker oxidative potential [42]. Moreover, other undesirable chlorinated byproducts (e.g., trihalomethanes and chloramines) may pose a health risk to the ecosystem [43].

The impact of sulfate concentration was further optimized (Fig. S11(b) in Appendix A). Increased aniline degradation from 2.6% to 100% is observed as the sulfate concentration increases from 0 to 50 $\text{mmol}\cdot\text{L}^{-1}$, resulting from the improved conductivity and from the presence of precursors for persulfate formation. Thus,

the effect on the aniline degradation kinetics of spiking different concentrations of nitrate together with 25 $\text{mmol}\cdot\text{L}^{-1}$ sulfate was examined. The results show a negligible effect of conductivity, as the removal efficiencies obtained for nitrate electrolytes of different molarities were very similar (Fig. S11(c) in Appendix A). Hence, the Na_2SO_4 electrolyte is an essential component to induce the generation of persulfate and reactive radicals.

3.6. Advantage of the flow-through design

Conventional batch electrochemistry is typically limited by mass transfer [8,10,20] due to its reliance on slow diffusion relative to electron transfer [44]. In stark contrast, the proposed electrochemical filtration system, in which water flows perpendicular to and through the porous filter electrodes, can be employed to overcome the mass transfer limitation. This forced convection, combined with the confinement effect of the solution within the electrode internal pores, collectively boosts the transfer of reactants and electrons at the membrane/solution interface [45,46]. This synergy also facilitates the intimate contact of reactants to maximally exploit the oxidation capacity of CNT-TiSO for persulfate synthesis, as well as the reducing capacity of Ti for radical production [47]. The experimental results confirm this demonstration, as a 2.3-fold increase in the aniline removal kinetics is observed for the flow-through configuration compared with a conventional batch mode (70.2% vs 30.5%) (Fig. S12(a) in Appendix A). This benefit is further enhanced by a decreased flow rate, as the resulting degradation efficiency reaches 70.2%, 85.5%, and 100% at flow rates of 3.0, 2.5, and 2.0 $\text{mL}\cdot\text{min}^{-1}$, respectively. This result can be attributed to an increased hydraulic residence time within the hybrid filter at a lower flow rate, which results in adequate contact between the generated reactive species and the aniline molecules [48]. Moreover, the effect of the initial aniline concentration on the degradation efficiency is displayed in Appendix A Fig. S12(b). Once the aniline concentration is below 0.1 $\text{mmol}\cdot\text{L}^{-1}$, complete aniline degradation can be achieved. However, a slight decrease in aniline degradation efficiency is observed with an increase in aniline concentration from 0.1 to 0.2 $\text{mmol}\cdot\text{L}^{-1}$. This decrease might be associated with competition for limited reactive sites on the filter surface at an elevated concentration of aniline.

3.7. Feasibility and practical considerations

Sulfates are ubiquitous in natural water bodies, with concentration that vary from dozens to hundreds of milligrams per liter ($\text{mg}\cdot\text{L}^{-1}$); thus, they can serve as an intrinsic sulfate source for the *in situ* production of persulfates and sulfate radicals. We have developed a sustainable reagent-free strategy for the electrochemical generation of $\text{SO}_4^{\cdot-}$. The economic aspect is an important factor in assessing the remediation techniques for practical application. The cost of this system has two predominant components: energy consumption and material cost. The proposed technology has no costs associated with the addition of chemical reagents, due to the ubiquitous presence of sulfates in water [49]. It has been estimated that 0.66 g of CNTs can form a 1- μm -thick layer over an area of 1 m^2 , implying a material cost of about 1.83 $\text{USD}\cdot\text{m}^{-2}$. In recent years, the price of CNTs has decreased remarkably due to advances in mass production technologies, which can overcome the limitations of cost budgets and technical obstacles [50]. Thus, the need for CNTs may not hinder the commercial application of the proposed technology. Importantly, the proposed electrochemical filtration process requires an energy consumption of only 0.00024 $\text{kW}\cdot\text{h}\cdot\text{L}^{-1}$ (Section S6 in Appendix A) at an anode potential of 2.0 V vs Ag/AgCl at 2.5 $\text{mA}\cdot\text{cm}^{-2}$ ($\sigma = 7240 \pm 100 \mu\text{S}\cdot\text{cm}^{-1}$), which is comparable to or even lower than various state-of-the-art aniline degradation processes (Table S1).

Furthermore, no obvious decrease in aniline degradation was observed over 9 h of continuous operation (Fig. S13 in Appendix A). To further explore the potential of system II for organic decontamination, four other refractory organic contaminants with varying molecular structures were tested (Table S2 in Appendix A). The obtained results suggest that all these contaminants—including SMX, methylene blue, methyl orange, tetracycline, and bisphenol A—can be effectively degraded by the proposed electrochemical filtration system by just a single pass through the system (all > 90%; Fig. S14(a) in Appendix A), indicating the wide applicability of the sulfate radical-mediated advanced oxidation processes. Moreover, the limited decrease in aniline removal in water from other sources (3.5% for tap water and 6.0% for lake water) compared with ultra-pure water within a hydraulic retention time of < 2 s is highly encouraging (Fig. S14(b) in Appendix A); this finding may be due to the slower reaction rate between $\text{SO}_4^{\cdot-}$ and natural organic matter ($k = 2.5 \times 10^7$ – $8.1 \times 10^7 \text{ L} \cdot (\text{mol} \cdot \text{s})^{-1}$) compared with the reaction rate between $\text{SO}_4^{\cdot-}$ and aniline ($k = 7.7 \times 10^9 \text{ L} \cdot (\text{mol} \cdot \text{s})^{-1}$). XRD and FESEM analyses of the CNT-TiSO nanohybrid filter before and after filtration suggest negligible changes to its surface chemistry, demonstrating the filter's excellent structural and chemical robustness, which ensures the continuous production of reactive species (Figs. S14(c) and (d) and S15 in Appendix A).

4. Conclusion

In summary, we have demonstrated a sustainable strategy to directly transform the ubiquitous sulfate anions in water into persulfate and then into highly reactive sulfate radicals via sequential electrochemistry. The proposed technology does not require the addition of any chemical reagents and is commercially viable. The underlying working mechanism was collectively unveiled based on theoretical calculation and experimental evidence. Under optimal conditions, the degradation and TOC removal efficiency of aniline reached 100% and 65%, respectively. Thanks to convection-enhanced mass transfer, the flow-through configuration outperforms conventional batch electrochemistry. The effectiveness of this excellent system can be maintained over a broad pH range, complex water matrices, and an array of refractory micropollutants. Encouragingly, the required electricity can be supplied by renewable energy resources (e.g., wind and solar) to further reduce greenhouse gas emissions from the power sector and help to address climate change. This work successfully implemented the green chemistry of sulfate-radical-mediated advanced oxidation processes to decontaminate diverse refractory micropollutants in water.

Acknowledgments

This work is supported by the National Natural Science Foundation of China (52170068 and U21A20161) and the Open Project of State Key Laboratory of Urban Water Resource and Environment, Harbin Institute of Technology (QAK202108).

Compliance with ethics guidelines

Wentian Zheng, Shijie You, Yuan Yao, Nanqi Ren, Bin Ding, Fang Li, and Yanbiao Liu declare that they have no conflict of interest or financial conflicts to disclose.

Appendix A. Supplementary data

Supplementary data to this article can be found online at <https://doi.org/10.1016/j.eng.2022.12.005>.

References

- [1] Luo Y, Guo W, Ngo HH, Nghiem LD, Hai FI, Zhang J, et al. A review on the occurrence of micropollutants in the aquatic environment and their fate and removal during wastewater treatment. *Sci Total Environ* 2014;473–474:619–41.
- [2] Li LF, Mao YX, Dong HY, Wang Y, Xu L, Liu SG, et al. The ultrafiltration process enhances antibiotic removal in the full-scale advanced treatment of drinking water. *Engineering* 2022. In press.
- [3] Jiang N, Shang R, Heijman SGJ, Rietveld LC. High-silica zeolites for adsorption of organic micro-pollutants in water treatment: a review. *Water Res* 2018;144:145–61.
- [4] Butkovskiy A, Jeremiasse AW, Hernandez Leal L, van der Zande T, Rijnaarts H, Zeeman G. Electrochemical conversion of micropollutants in gray water. *Environ Sci Technol* 2014;48(3):1893–901.
- [5] Radjenovic J, Petrovic M. Removal of sulfamethoxazole by electrochemically activated sulfate: implications of chloride addition. *J Hazard Mater* 2017;333:242–9.
- [6] Liu YM, Zhang YJ, Cheng K, Quan X, Fan XF, Su Y, et al. Selective electrochemical reduction of carbon dioxide to ethanol on a boron- and nitrogen-Co-doped nanodiamond. *Angew Chem Int Ed Engl* 2017;56(49):15607–11.
- [7] Sgroi M, Roccaro P, Oelker GL, Snyder SA. N-nitrosodimethylamine formation upon ozonation and identification of precursors source in a municipal wastewater treatment plant. *Environ Sci Technol* 2014;48(17):10308–15.
- [8] Farhat A, Keller J, Tait S, Radjenovic J. Removal of persistent organic contaminants by electrochemically activated sulfate. *Environ Sci Technol* 2015;49(24):14326–33.
- [9] Liu GS, You SJ, Tan Y, Ren NQ. In situ photochemical activation of sulfate for enhanced degradation of organic pollutants in water. *Environ Sci Technol* 2017;51(4):2339–46.
- [10] Liu YM, Fan XF, Quan X, Fan YF, Chen S, Zhao XY. Enhanced perfluorooctanoic acid degradation by electrochemical activation of sulfate solution on B/N codoped diamond. *Environ Sci Technol* 2019;53(9):5195–201.
- [11] Chen WM, Luo YF, Ran G, Li QB. An investigation of refractory organics in membrane bioreactor effluent following the treatment of landfill leachate by the $\text{O}_3/\text{H}_2\text{O}_2$ and MW/PS processes. *Waste Manag* 2019;97:1–9.
- [12] Wang F, Wu CW, Li QB. Treatment of refractory organics in strongly alkaline dinitrodiazophenol wastewater with microwave irradiation-activated persulfate. *Chemosphere* 2020;254:126773.
- [13] Li XY, Jie BR, Lin HD, Deng ZP, Qian JY, Yang YQ, et al. Application of sulfate radicals-based advanced oxidation technology in degradation of trace organic contaminants (TrOCs): recent advances and prospects. *J Environ Manage* 2022;308:114664.
- [14] Miklos DB, Remy C, Jekel M, Linden KG, Drewes JE, Hübner U. Evaluation of advanced oxidation processes for water and wastewater treatment - a critical review. *Water Res* 2018;139:118–31.
- [15] Zhu YQ, Chen S, Quan X, Zhang YB. Cobalt implanted TiO_2 nanocatalyst for heterogeneous activation of peroxymonosulfate. *RSC Adv* 2013;3:520–5.
- [16] Hu PD, Long MC. Cobalt-catalyzed sulfate radical-based advanced oxidation: a review on heterogeneous catalysts and applications. *Appl Catal B* 2016;181:103–17.
- [17] Zheng ZZ, Eglin D, Alini M, Richards GR, Qin L, Lai YX. Visible light-induced 3D bioprinting technologies and corresponding bioink materials for tissue engineering: a review. *Engineering* 2021;7(7):966–78.
- [18] Ren W, Zhang QM, Cheng C, Miao F, Zhang H, Luo XB, et al. Electro-induced carbon nanotube discrete electrodes for sustainable persulfate activation. *Environ Sci Technol* 2022;56(19):14019–29.
- [19] de F, Araújo KC, de P, Barreto JP, Cardozo JC, dos Santos EV, de Araújo DM, Martínez-Huitle CA. Sulfate pollution: evidence for electrochemical production of persulfate by oxidizing sulfate released by the surfactant sodium dodecyl sulfate. *Environ Chem Lett* 2018;16(2):647–52.
- [20] Matzek LW, Tipton MJ, Farmer AT, Steen AD, Carter KE. Understanding electrochemically activated persulfate and its application to ciprofloxacin abatement. *Environ Sci Technol* 2018;52(10):5875–83.
- [21] Davis J, Baygents JC, Farrell J. Understanding persulfate production at boron doped diamond film anodes. *Electrochim Acta* 2014;150:68–74.
- [22] Chen Z, Geng SP, Xiao J, Zhao FY, Wang K, Wang Y, et al. Understanding the selectivity trend of water and sulfate ($\text{SO}_4^{\cdot-}$) oxidation on metal oxides: on-site synthesis of persulfate, H_2O_2 for wastewater treatment. *Chem Eng J* 2022;431:134332.
- [23] Marenich AV, Cramer CJ, Truhlar DG. Universal solvation model based on solute electron density and on a continuum model of the solvent defined by the bulk dielectric constant and atomic surface tensions. *J Phys Chem B* 2009;113(18):6378–96.
- [24] Gao YF, Zhang JN, Bai XF, You SJ. Monolithic ceramic electrode for electrochemical deactivation of *Microcystis aeruginosa*. *Electrochim Acta* 2018;259:410–8.
- [25] Pei SZ, Shi H, Zhang JN, Wang SL, Ren NQ, You SJ. Electrochemical removal of tetrabromobisphenol A by fluorine-doped titanium suboxide electrochemically reactive membrane. *J Hazard Mater* 2021;419:126434.
- [26] Teng J, Liu GS, Liang J, You SJ. Electrochemical oxidation of sulfadiazine with titanium suboxide mesh anode. *Electrochim Acta* 2020;331:135441.
- [27] Wu T, Zhao GH, Lei YZ, Li PQ. Distinctive tin dioxide anode fabricated by pulse electrodeposition: high oxygen evolution potential and efficient electrochemical degradation of fluorobenzene. *J Phys Chem C* 2011;115(10):3888–98.

- [28] Bai P, Bazant MZ. Charge transfer kinetics at the solid-solid interface in porous electrodes. *Nat Commun* 2014;5(1):3585.
- [29] Lei Y, Chen CS, Tu YJ, Huang YH, Zhang H. Heterogeneous degradation of organic pollutants by persulfate activated by CuO-Fe₃O₄: mechanism, stability, and effects of pH and bicarbonate ions. *Environ Sci Technol* 2015;49(11):6838–45.
- [30] Liu GS, Zhou H, Teng J, You SJ. Electrochemical degradation of perfluorooctanoic acid by macro-porous titanium suboxide anode in the presence of sulfate. *Chem Eng J* 2019;371:7–14.
- [31] Chen WS, Huang CP. Mineralization of aniline in aqueous solution by electrochemical activation of persulfate. *Chemosphere* 2015;125:175–81.
- [32] Matzek LW, Carter KE. Activated persulfate for organic chemical degradation: a review. *Chemosphere* 2016;151:178–88.
- [33] Shi XJ, Siahrostami S, Li GL, Zhang YR, Chakthranont P, Studt F, et al. Understanding activity trends in electrochemical water oxidation to form hydrogen peroxide. *Nat Commun* 2017;8(1):701.
- [34] Su HL, Christodoulatos C, Smolinski B, Arienti P, O'Connor G, Meng XG. Advanced oxidation process for DNAN using UV/H₂O₂. *Engineering* 2019;5(5):849–54.
- [35] Jin LM, You SJ, Ren NQ, Ding B, Liu YB. Mo vacancy-mediated activation of peroxymonosulfate for ultrafast micropollutant removal using an electrified MXene filter functionalized with Fe single atoms. *Environ Sci Technol* 2022;56(16):11750–9.
- [36] Su LN, Wang PF, Ma XL, Wang JH, Zhan SH. Regulating local electron density of iron single sites by introducing nitrogen vacancies for efficient photo-Fenton process. *Angew Chem Int Ed Engl* 2021;60(39):21261–6.
- [37] Oh WD, Dong ZL, Ronn G, Lim TT. Surface-active bismuth ferrite as superior peroxymonosulfate activator for aqueous sulfamethoxazole removal: Performance, mechanism and quantification of sulfate radical. *J Hazard Mater* 2017;325:71–81.
- [38] Zhang YJ, Zhang Q, Peng HJ, Zhang WL, Li M, Feng JP, et al. The changing C/N of aggressive aniline: metagenomic analysis of pollutant removal, metabolic pathways and functional genes. *Chemosphere* 2022;309(Pt 1):136598.
- [39] Guo DL, You SJ, Li F, Liu YB. Engineering carbon nanocatalysts towards efficient degradation of emerging organic contaminants via persulfate activation: a review. *Chin Chem Lett* 2022;33(1):1–10.
- [40] Wu YL, Bianco A, Brigante M, Dong WB, de Sainte-Claire P, Hanna K, et al. Sulfate radical photogeneration using Fe-EDDS: influence of critical parameters and naturally occurring scavengers. *Environ Sci Technol* 2015;49(24):14343–9.
- [41] Liu FQ, Wang ZY, You SJ, Liu YB. Electrogenerated quinone intermediates mediated peroxymonosulfate activation toward effective water decontamination and electrode antifouling. *Appl Catal B* 2023;320:121980.
- [42] Lin MH, Bulman DM, Remucal CK, Chaplin BP. Chlorinated byproduct formation during the electrochemical advanced oxidation process at Magnéli phase Ti₄O₇ electrodes. *Environ Sci Technol* 2020;54(19):12673–83.
- [43] Florentin A, Hautemanière A, Hartemann P. Health effects of disinfection by-products in chlorinated swimming pools. *Int J Hyg Environ Health* 2011;214(6):461–9.
- [44] Guo DL, Liu YB, Ji HD, Wang CC, Chen B, Shen CS, et al. Silicate-enhanced heterogeneous flow-through electro-Fenton system using iron oxides under nanoconfinement. *Environ Sci Technol* 2021;55(6):4045–53.
- [45] Pei SZ, You SJ, Zhang JN. Application of pulsed electrochemistry to enhanced water decontamination. *ACS EST Engg* 2021;1(11):1502–8.
- [46] Pei SZ, Wang Y, You SJ, Li Z, Ren NQ. Electrochemical removal of chlorophenol pollutants by reactive electrode membranes: scale-up strategy for engineered applications. *Engineering* 2022;9:77–84.
- [47] Liu YB, Gao GD, Vecitis CD. Prospects of an electroactive carbon nanotube membrane toward environmental applications. *Acc Chem Res* 2020;53(12):2892–902.
- [48] Zheng WT, Liu YB, Liu W, Ji HD, Li F, Shen CS, et al. A novel electrocatalytic filtration system with carbon nanotube supported nanoscale zerovalent copper toward ultrafast oxidation of organic pollutants. *Water Res* 2021;194:116961.
- [49] Oliveira FR, Surendra KC, Jaisi DP, Lu H, Unal-Tosun G, Sung S, et al. Alleviating sulfide toxicity using biochar during anaerobic treatment of sulfate-laden wastewater. *Bioresour Technol* 2020;301:122711.
- [50] Liu YB, Liu FQ, Ding N, Hu XM, Shen CS, Li F, et al. Recent advances on electroactive CNT-based membranes for environmental applications: the perfect match of electrochemistry and membrane separation. *Chin Chem Lett* 2020;31(10):2539–48.